



A method for simulating Atomic Force Microscope nanolithography in the Level Set framework

Lado Filipovic*, Siegfried Selberherr

Institute for Microelectronics, TU Wien, Gußhausstraße 27–29/E360, A-1040 Wien, Austria

ARTICLE INFO

Article history:

Received 20 December 2012

Received in revised form 30 January 2013

Accepted 14 February 2013

Available online 7 March 2013

Keywords:

Topography simulation

Level Set

Monte Carlo

Local anodic oxidation

Atomic Force Microscope

Oxide nanodots

ABSTRACT

During the last decades it has been shown that the Atomic Force Microscope (AFM) can be used in non-contact mode as an efficient lithographic technique capable of manufacturing nanometer sized devices on the surface of a silicon wafer. The AFM nanooxidation approach is based on generating a potential difference between a cantilever needle tip and a silicon wafer. A water meniscus builds up between the tip and the wafer, resulting in a medium for oxyions to move due to the high electric field in the region. A simulator for nanooxidation with a non-contact AFM, implemented in a Level Set environment, was developed. The presented simulator implements the growth of thicker oxides by analyzing the potential, electric field, and ion concentrations at the ambient/oxide and oxide/silicon interfaces, while the growth of thin oxides assumes a single liquid/silicon interface, which is modeled as an infinitely long conducting plane. The nanodot shapes have been shown to follow the electric field and hence the surface charge distribution shape; therefore, a Monte Carlo particle distribution for the surface charge density is generated for two-dimensional and three-dimensional topography simulations in a Level Set framework.

© 2013 Elsevier B.V. All rights reserved.

1. Introduction

In order to continue the miniaturization trend in the semiconductor industry, novel processing techniques are being introduced in order to replace traditional optical and electron beam lithographies. One such attempt to pattern nanosized sections of a silicon surface with locally grown silicon dioxide is Local Oxidation Nanolithography (LON) [1,2]. The invention of the Scanning Tunneling Microscope (STM) in the 1980s allowed for the visualization of nanosized deformations in a conductor or semiconductor surface [3]. Soon thereafter, the Atomic Force Microscope (AFM) was found to perform the same surface imaging as an STM at a much finer resolution (0.01 nm depth) [4]. The use of these tools for the LON of silicon surfaces followed, with the discovery that a charged needle tip can generate a high electric field when brought near a semiconductor surface, whether it be with a STM [5] or an AFM [6]. The main advantages of AFM over STM nanooxidation are a much finer control of the tip-surface distance and the ability to read back the generated topography directly, while the STM cannot differentiate between the grown oxide and ambient environments. This led to a growing interest in localized nanooxidation with a charged AFM needle, which can be operated in contact mode, intermittent contact mode, or non-contact mode (NCM). NCM operation generates the finest resolution and has the highest reproducibility since this

type of operation causes the least damage to the integrity of the AFM needle. A typical AFM setup is depicted in Fig. 1.

1.1. Non-contact mode nanolithography

In 1998, Garcia et al. demonstrated that the AFM needle need not directly strike or contact the silicon surface in order for oxidation to proceed [7]. Bringing the charged needle close to the silicon wafer in a humid environment was enough to generate a strong electric field in the region, which is the main cause for ion generation and silicon oxidation. The procedure required in order to generate a single oxide nanodot using an AFM in NCM is laid out in [8]:

- (1) The AFM needle tip is oscillated above the sample surface, followed by the application of the bias voltage pulse.
- (2) The oscillator amplitude is reduced by the electrostatic interaction, which deflects the AFM needle tip position and modifies the AFM cantilever's resonant frequency.
- (3) The bias voltage is turned off; however, the AFM cantilever oscillation remains reduced due to the capillary force of the water meniscus.
- (4) Finally, the tip is lifted away from the water meniscus, allowing for its oscillations to return to their initial amplitude.

The oxidation reaction, including holes (h^+) and electrons (e^-), at the anode end (silicon surface) is

* Corresponding author. Tel.: +43 1 58801 36036; fax: +43 1 58801 36099.

E-mail addresses: filipovic@iue.tuwien.ac.at (L. Filipovic), selberherr@iue.tuwien.ac.at (S. Selberherr).

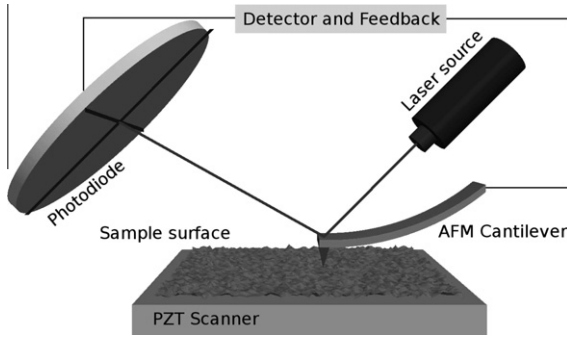
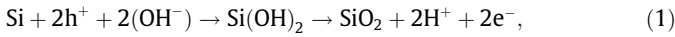


Fig. 1. Typical AFM schematic for surface imaging.



while the reaction at the cathode end (AFM needle tip) is



Our work deals with the generation of models for silicon nanopatterning using an AFM in NCM and the associated topography simulations in a Level Set (LS) framework. Recently, the AFM has been used in order to perform nano-oxidation on doped silicon and silicon carbide substrates [9].

2. Level Set method

In order to simulate topography modifications a method which is able to describe geometric deformations over time is required. In literature, there are simulations of AFM oxidation based on the surface chemistry [10] and mathematical models exist which attempt to describe the growth of nanodots and nanowires [11,12]. It is the goal of this work to generate a topography simulator for AFM oxidation which allows for the process to be incorporated within a chain of process simulations through its integration in a LS framework. The LS method allows for the tracking of surface modifications under a given velocity in the surface normal direction [13]. In short, the LS method describes a movable surface $\mathcal{S}(t)$ as the zero LS of a continuous function $\Phi_{\text{LS}}(\vec{x}, t)$ defined on the entire simulation domain,

$$\mathcal{S}(t) = \{\vec{x} : \Phi_{\text{LS}}(\vec{x}, t) = 0\}. \quad (3)$$

The continuous function $\Phi_{\text{LS}}(\vec{x}, t)$ is obtained using a signed distance transform

$$\Phi_{\text{LS}}(\vec{x}, t = 0) := \begin{cases} -\min_{\vec{x}' \in \mathcal{S}(t=0)} \|\vec{x} - \vec{x}'\| & \text{if } \vec{x} \in \mathcal{M}(t=0), \\ +\min_{\vec{x}' \in \mathcal{S}(t=0)} \|\vec{x} - \vec{x}'\| & \text{else,} \end{cases} \quad (4)$$

where \mathcal{M} is the material described by the LS surface $\Phi_{\text{LS}}(\vec{x}, t = 0)$. The implicitly defined surface $\mathcal{S}(t)$ describes a surface evolution, driven by a scalar velocity $V(\vec{x})$, using the LS equation

$$\frac{\partial \Phi_{\text{LS}}}{\partial t} + V(\vec{x}) \|\nabla \Phi_{\text{LS}}\| = 0. \quad (5)$$

In order to find the final location of the evolved surface, the velocity field $V(\vec{x})$ must be found. For a detailed description of the core LS framework implemented using a Sparse Field Method and a Hierarchical Run Length Encoded data structure which is used in order to generate the presented simulations, refer to [14]. Within the scope of this work, nanopatterns are simulated in the LS framework through the generation of the appropriate velocity field $V(\vec{x})$.

The velocity field describes the evolution of the LS surface along its normal direction. However, when the velocity of nanodot growth is given in the vertical direction only, using an asymptotic

method from [12], the velocity field $V(\vec{x})$ from (5) must be adjusted. In three dimensions, the direction of the velocity is given by the surface normal at \vec{x} , $\vec{n}(\vec{x})$. The LS method allows for a straight forward description of the normalized surface normals

$$\vec{n}(\vec{x}) = \frac{\nabla \Phi_{\text{LS}}}{\|\nabla \Phi_{\text{LS}}\|}. \quad (6)$$

However, if the required velocity should be directed in a single axial direction, such as the z -direction (001), then the velocity field is applied only in that direction, meaning

$$V_x(\vec{x}) = 0; \quad V_y(\vec{x}) = 0; \quad V_z(\vec{x}) = V_c(\vec{x}), \quad (7)$$

where $V_i(\vec{x})$ are components of a vector representation of the velocity field $V(\vec{x}) = (V_x(\vec{x}), V_y(\vec{x}), V_z(\vec{x}))$ and $V_c(\vec{x})$ is the calculated vertical velocity for the nanodot growth. Therefore, when a method such as the one presented in [12] is used to find the vertical rate of growth of the nanodot, (7) can be used to combine the desired model with the LS framework.

The LS method is commonly used to simulate topography evolution after the application of one or several semiconductor processing steps [15,16]. The ability to introduce novel mathematical models for nano-oxidation of silicon surfaces in a LS environment means that nano-oxidation simulations can be performed alongside a wide range of semiconductor processing steps. The LS approach is also a very powerful method by which a topography evolution over time can be visualized and manipulated with further processing steps.

3. Electric field effects during LON

Fig. 2 shows a model of a hemispherical needle tip with radius a , located at a distance L away from the silicon surface. As the oxide grows, the ambient/oxide interface is positioned at location h and the oxide/silicon interface is at location $-f$. The locations h and f depend on the radial distance from the AFM needle tip and the total oxide thickness is given by $t_{\text{ox}} = h + f$. The region depicted by ξ is used to denote a thin layer to account for the rapid buildup of space charge near the oxide/silicon interface.

3.1. Ambient water layer transport

Due to the applied potential between the needle and silicon substrate, a strong electric field is formed, which causes the generation of hydroxide ions (OH^-) at the AFM tip [12]. The applied voltage V_b is prescribed at location $z = L$, while the dot charge Q is located at $z = L + a$. In order to calculate the electric potential,

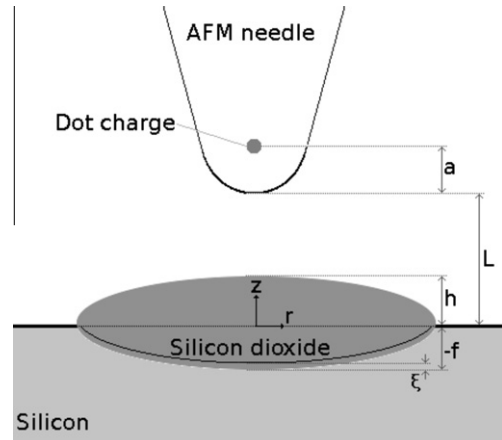


Fig. 2. Schematic of the model for a hemispherical needle tip.

electric field, and surface charge densities in the region where the charged AFM needle is applied, a semi-infinite water layer is assumed. A water bridge forms as the charged AFM needle is brought near the silicon surface. The potential through the liquid ambient for a semi-infinite water layer is given by

$$V_L = \frac{Q}{4\pi\epsilon_L} \left[\frac{1}{\sqrt{r^2 + (z-L-a)^2}} + \frac{1}{\sqrt{r^2 + (z+L+a)^2}} \right], \quad (8)$$

where ϵ_L is the permittivity in the liquid. The electric field along the z -direction is found using $E_L = -\nabla V_L$, giving

$$E_L = \frac{Q}{4\pi\epsilon_L} \left[\frac{L+a-z}{(r^2 + (L+a-z)^2)^{3/2}} - \frac{L+a+z}{(r^2 + (L+a+z)^2)^{3/2}} \right]. \quad (9)$$

The value of Q is found by noting that the voltage is V_b at $z = L$ during oxide growth.

$$Q = \frac{-2\pi\epsilon_L V_b a(a+2L)}{a+L}. \quad (10)$$

For the presented simulations it is assumed that the location of the AFM needle does not change as the oxide height is increased. Therefore, $V_L(z=L) = V_b$ for all time t .

The ions move along the electric field lines through the water meniscus ambient towards the ambient/oxide interface. The ion concentration and potential at the ambient side of the interface is preserved, while a Neumann boundary condition is applied

$$V_L = V_O \quad \text{and} \quad \frac{\delta V_L}{\delta z} = E_L = 0 \quad \text{at} \quad z = h, \quad (11)$$

where V_L is the voltage in the liquid ambient, V_O is the voltage in the oxide region, and E_L is the electric field in the liquid ambient [12].

3.2. Oxide layer transport

The oxide layer is effectively divided between the volume above and below the space charge trapping layer ξ . The potential can be viewed as V_O^+ above the trapping region and V_O^- within the trapping region, with a boundary condition $V_O^- = 0$ at $z = -f$. Across the trapping interface, the potential is preserved

$$V_O^+ = V_O^-, \quad \text{at} \quad z = -f + \xi, \quad (12)$$

where the potential is assumed to have a linear dependence on z , resulting in a constant value for the electric field E_O .

$$\frac{\delta^2 V_O^+}{\delta z^2} = \frac{\delta E_O^+}{\delta z} = 0, \quad \frac{\delta^2 V_O^-}{\delta z^2} = \frac{\delta E_O^-}{\delta z} = 0. \quad (13)$$

The potentials within the oxide layer V_O^+ and V_O^- are derived in [12], while the electric field within the region is found by taking the negative derivative in the z direction, resulting in

$$E_O^+ = -\frac{C(f+h-\xi) + V^*}{f+h} \quad (14)$$

and

$$E_O^- = -\frac{V^* - C\xi}{f+h} \quad (15)$$

where V^* is the initial voltage at the liquid/oxide interface before any new oxide growth, and $C = qN_A A / \epsilon_O$, where q is the elementary charge, N_A is Avogadro's number, A is the concentration of trap sites, and ϵ_O is the permittivity in the oxide.

The ion concentration at the oxide/silicon interface O_O^- is the main factor which determines the oxide growth rate. The rate is calculated by solving for the particle currents in the liquid and

oxide, followed by solving for the ion concentrations. The boundary conditions which govern the ion flux and ion concentrations at the liquid/oxide, oxide/trap site, and oxide trap site/silicon interfaces are given in [12]. A solution for O_O^- is calculated, and the rate of the oxide expansion into the silicon is then found using

$$\frac{df}{dt} = \frac{K_s O_O^-}{\rho_s} \quad \text{at} \quad z = -f, \quad (16)$$

where K_s is the reaction rate constant between hydroxyls (OH^-) and substrate and ρ_s is the density of silicon. It is important to note that O_O^- depends on many ambient factors, as well as the location of all interfaces. Due to its dependence on f , the growth rate will change during the oxidation process due to the oxide growth. In order to find the rate at which the ambient/oxide interface h grows, it is assumed that a typical oxidation process occurs, meaning that h is proportional to f depending on the difference in the oxide and silicon densities:

$$h = f \left(\frac{\rho_s}{\rho_o} - 1 \right) \quad \text{and} \quad \frac{dh}{dt} = \frac{df}{dt} \left(\frac{\rho_s}{\rho_o} - 1 \right), \quad (17)$$

where ρ_o is the density of the grown silicon dioxide.

4. Modeling nanodot growth during LON

As suggested in [12], an initial oxide thickness of 3.6 nm is assumed by assigning an initial location of $f = 1.5$ nm and $h = 2.1$ nm. The initial geometry is also generated to reflect this initial oxide layer, shown in Fig. 3.

When simulating within the LS environment, the velocity field $V(\vec{x})$ is deduced from the combined surface rates. However, the exact global locations of the interfaces $-f$ and h are not known. Therefore, in order to simulate the nanodot growth, (16) and (17) are used to calculate the required rates, while the interface locations $-f$ and h must be found in a different manner.

The full set of equations is solved for several values of f in order to estimate its dependence on $\frac{df}{dt}$. Fig. 4 shows how the rate of oxide growth is decreased as the oxide thickness is increasing. The process-dependent variables during the simulation are given by: $V_b = 10$ V, $a = 25$ nm, $L = 20$ nm, $r = 0$ nm. All other variables are assumed to be static and not modifiable; those are given in [12]. An empirical equation for $\frac{df}{dt}$ which closely matches the calculated result is

$$\frac{df}{dt} = \frac{A}{f+B}, \quad (18)$$

where A (nm^2/s) and B (nm) are process-dependent parameters, adjusted by modifying V_b , a , L , and r .

Eq. (18) can be integrated to solve for f in terms of time t

$$f(t) = -B + \sqrt{B^2 + 2A(t+\tau)}, \quad (19)$$

where τ (s) is a constant meant to deal with the initial oxide growth f_0 given by

$$\tau = \frac{B}{A} f_0 + \frac{1}{2A} f_0^2. \quad (20)$$

The dependence of the applied voltage V_b , a , L , and r on the values of A and B has been examined as shown in Fig. 5. These dependences were taken into account when calculating the value of f required in the equation for the ion concentration O_O^- and hence the growth rate.

4.1. Nanodot simulations

With an applied voltage $V_b = 10$ V, $a = 25$ nm, and $L = 20$ nm, a simulation of the nanodot growth was carried out for 3 s on the

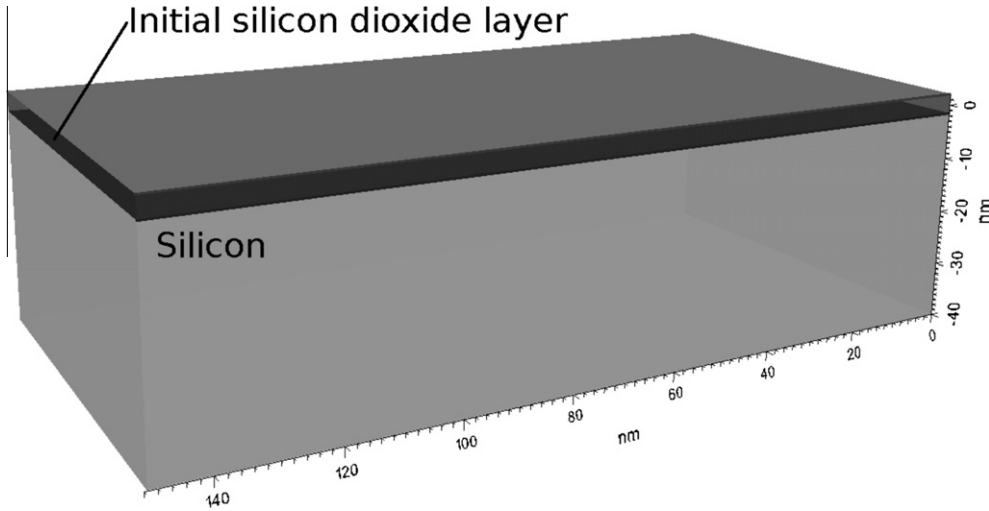


Fig. 3. Initial geometry with an initial $t_{ox} = 3.6$ nm.

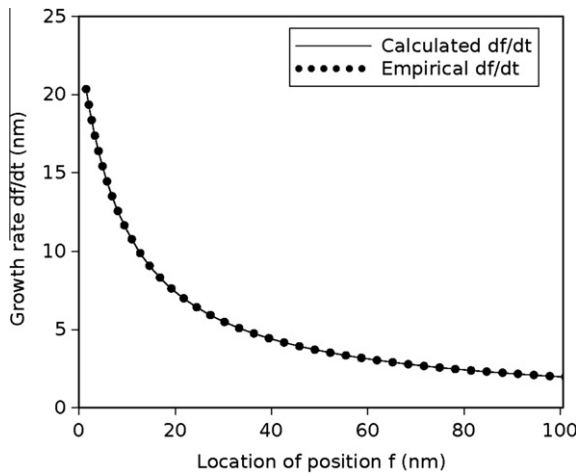


Fig. 4. Comparison between calculated $\frac{df}{dt}$ (16) and the empirical estimate (18).

geometry from Fig. 3. Fig. 6 shows the cross section of this simulation, while Fig. 7a and b shows the three-dimensional view of the nanodot after 1 s and 2 s, respectively.

The simulations include the reduced oxidation rate as the thickness of the oxide increases. The main parameter which decides the nanodot shape is the applied electric field. With the presented methods, relatively large nanodots with heights of tens or hundreds of nanometers can be simulated. When such high nanodots are required, the interaction between different materials and the potential, electric field strength, and ion concentrations at all material boundaries must be analyzed in order to accurately predict the ion concentration at the oxide/silicon interface.

When the initial oxide thickness is removed prior to LON and when only a slight burst (<10 ms) is used instead of a long process time of several seconds, the effective distance between the boundaries is too small to significantly influence the nanodot shape. Therefore, the shape will directly follow the ion concentration or density of charges at the silicon surface. Additionally, the equations which govern the voltage and electric field distributions in the liquid must be adjusted so that at $z = 0$, the potential $V_L = 0$. The simulation of nanodots with a height not larger than several nanometers after applying a voltage bias for fractions of milliseconds are discussed in the following section.

5. Empirical models for nano-scale oxidation

Empirical equations describing the influence of the bias voltage V_b , pulse time t , and relative air humidity (RAH) h_r on the height (H) and full width at half maximum (FWHM) of a nanodot generated using an AFM in NCM have been previously reported in [17] as

$$H = [H_0(V_b) + H_1(V_b) \ln(t)] \cdot [0.00037 h_r^2 - 0.019 h_r + 0.928], \quad (21)$$

where

$$\begin{aligned} H_0(V_b) &= -2.1 + 0.5 V_b - 0.006 V_b^2, \\ H_1(V_b) &= 0.1 + 0.03 V_b - 0.0005 V_b^2, \end{aligned} \quad (22)$$

and

$$\text{FWHM} = [W_0(V_b) + W_1(V_b) \ln(t)] \cdot [0.019 h_r - 0.051], \quad (23)$$

where

$$\begin{aligned} W_0(V_b) &= 11.6 + 9 V_b, \\ W_1(V_b) &= 2.7 + 0.9 V_b, \end{aligned} \quad (24)$$

and where H and FWHM are given in nanometers, while V_b , t , and h_r are given in volts, seconds, and percent, respectively.

5.1. Nanodot modeling using the Monte Carlo method

Our simulator is implemented by first calculating the shape of the nanodot with the mentioned empirical equations. Afterwards, a given number of particles is distributed above the silicon surface, with their position following the pattern of the desired surface deformation. Finally, each particle is accelerated towards the surface, causing it to collide with the wafer. Upon impact, the silicon dioxide is advanced deeper into the silicon through the interface f , while it simultaneously grows into the ambient through the interface h . The interface f represents the interface between the silicon and silicon dioxide. As oxide is grown, f is advanced in the negative direction and h in the positive direction at rates which depend on the total oxide growth rate and the densities of silicon and silicon dioxide, as shown in (17). The result is an oxide nanodot or nanowire having the desired height and width, depending on the process parameters which are of voltage, time, and humidity. Some authors approximate the final oxide dot topography with a Gaussian curvature [18], while some suggest a Lorentzian profile [19];

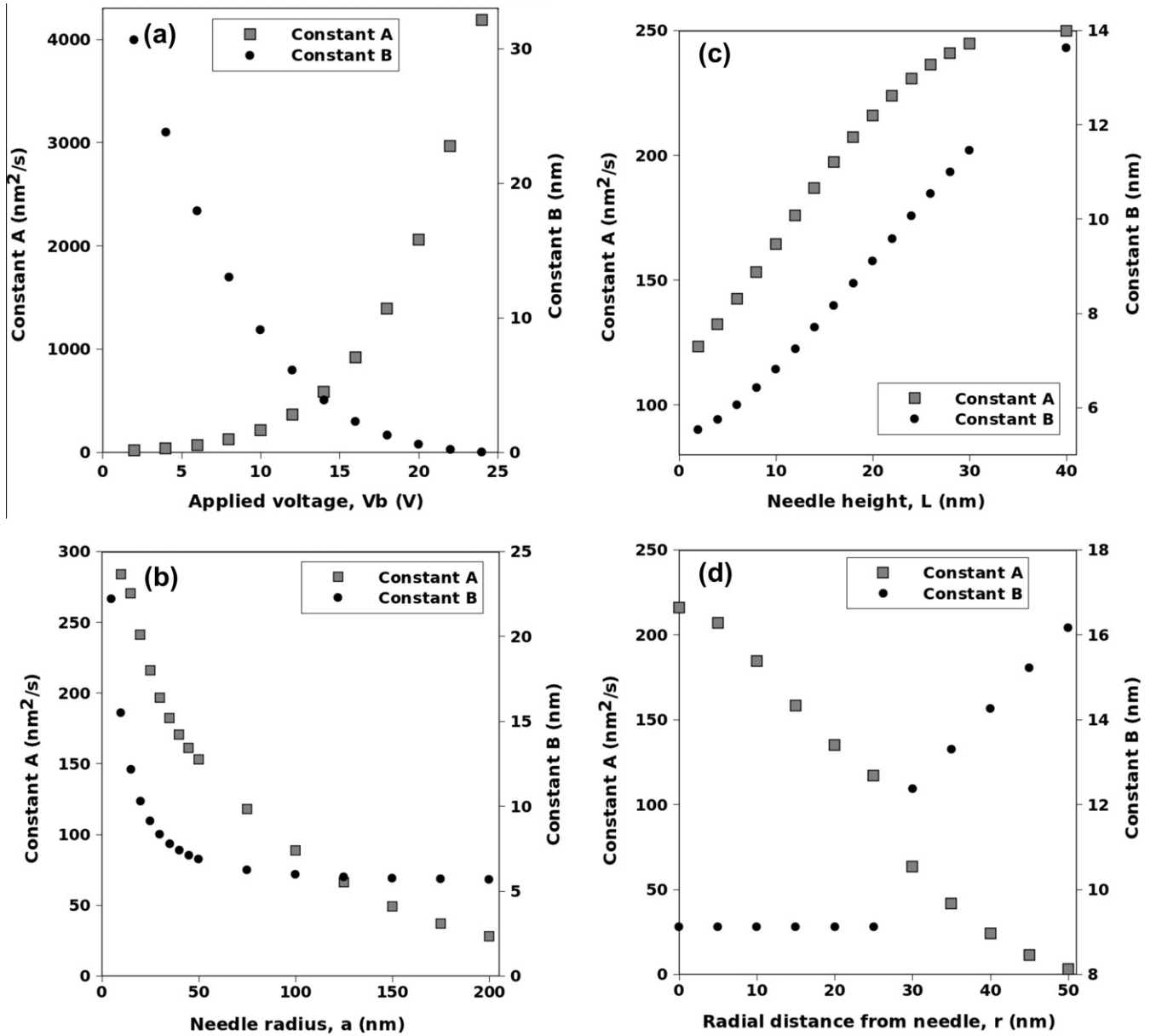


Fig. 5. Effects of the applied voltage V_b , AFM needle tip radius a , AFM needle height L , and the radial distance from the needle tip r on the constants A and B from (18).

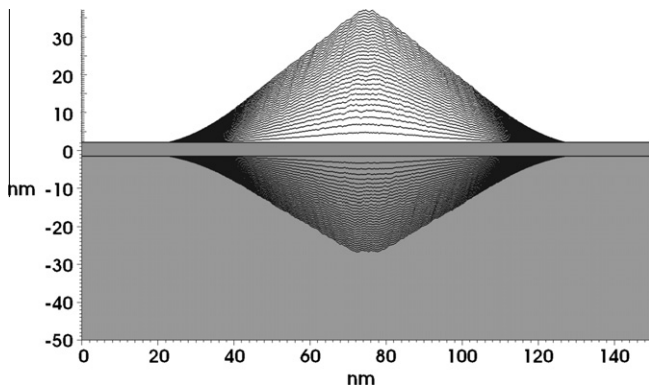


Fig. 6. Diagonal cross-section of nanodot growth for 3 s with 0.1 s intervals shown with $V_b=10$ V, $a=25$ nm, and $L=20$ nm.

however, with the knowledge that the curvature of the nanodot is governed by the electric field, and thereby the surface charge

density (SCD), it would be advantageous to have a particle distribution which follows the SCD. The flow of the presented simulator is sketched in Fig. 8 where it is shown that particles can follow a Gaussian, Lorentzian [17], or a SCD [20] distribution.

6. Monte Carlo particle distribution

The implementation of Monte Carlo particle distributions for the simulation of LON using a hemispherical as well as rough/blunt AFM needle tip are presented in this section.

6.1. Hemispherical needle tip

As discussed in the previous sections, the model representing the shape of a hemispherical AFM generated nanodot follows the SCD distribution which is derived by replacing the AFM needle tip with an effective point source Q and the silicon substrate surface by an infinitely long conducting plane. The image charge

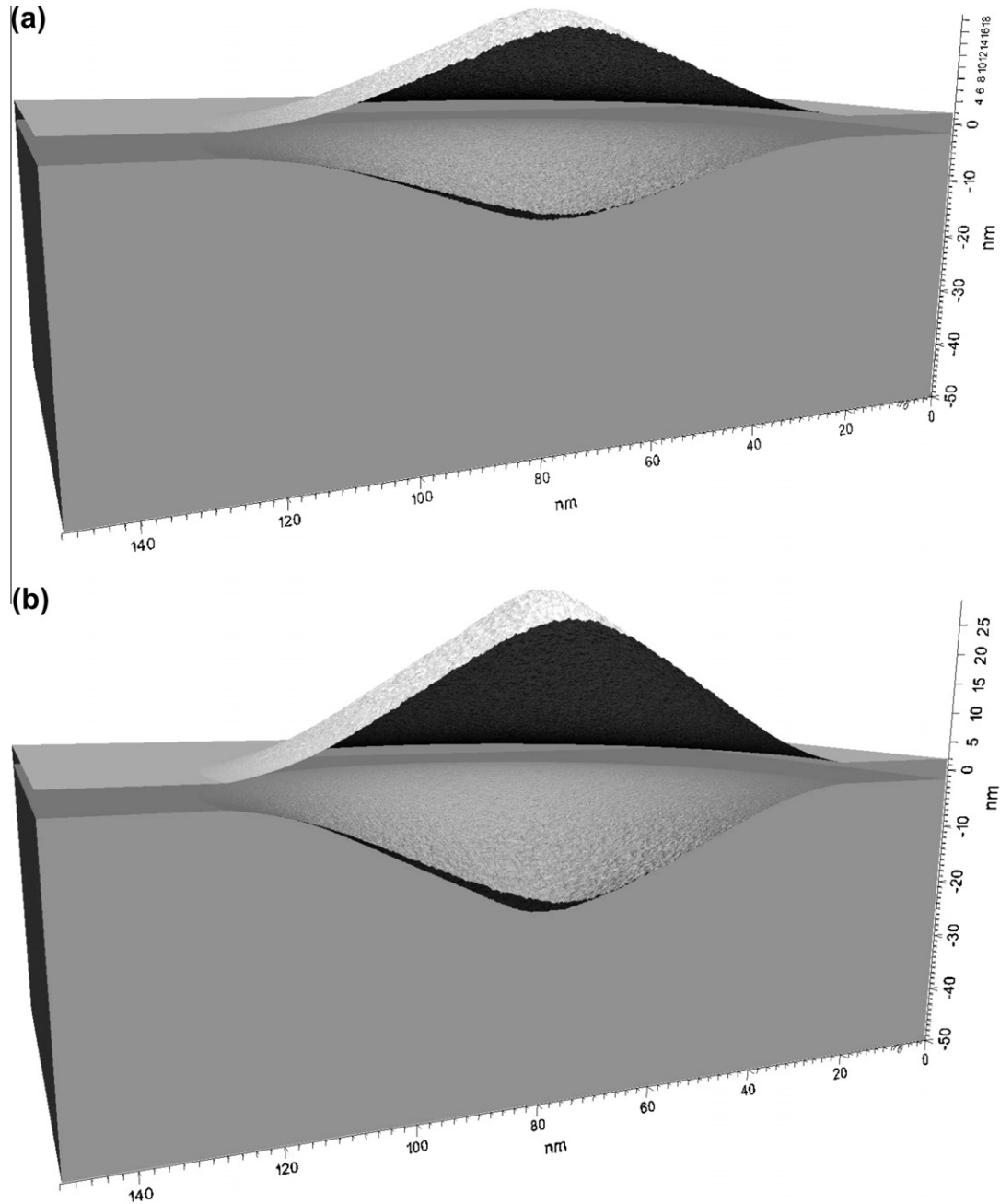


Fig. 7. Three-dimensional view of a nanodot which is grown for (a) 1 s and (b) 2 s with $V_b=10$ V, $a=25$ nm, and $L=20$ nm.

method [21] is applied in order to find the voltage at every location in the water meniscus region $\vec{p}(r, z)$:

$$V_L(\vec{p}) = \frac{Q}{4\pi\epsilon_L} \left[\frac{1}{\sqrt{r^2 + (z - L - a)^2}} - \frac{1}{\sqrt{r^2 + (z + L + a)^2}} \right]. \quad (25)$$

The equation has been reformulated to reflect a vanishing potential at the location of the wafer surface, effectively the infinitely long conducting plane. Knowing that $V_L(\vec{p}) = V_b$ at $z = L$, Q can be found

$$Q = \frac{2\pi\epsilon_L V_b a(a + 2L)}{L}. \quad (26)$$

The electric field in the z direction is found to be

$$E_L(\vec{p}) = \frac{Q}{4\pi\epsilon_L} \left[\frac{z - L - a}{(r^2 + (z - L - a)^2)^{3/2}} - \frac{z + L + a}{(r^2 + (z + L + a)^2)^{3/2}} \right]. \quad (27)$$

The induced SCD on the surface is represented as

$$\sigma(r, 0) = \epsilon_L E_L(r, 0). \quad (28)$$

Setting Q at a height D above the surface means that $D = L + a$, leading to the expression for the SCD

$$\sigma(r, 0) = \frac{-DQ}{2\pi(r^2 + D^2)^{3/2}}. \quad (29)$$

6.1.1. One-dimensional surface charge density distribution

When performing AFM nanodot simulations for a two-dimensional model, a one-dimensional particle distribution is required.

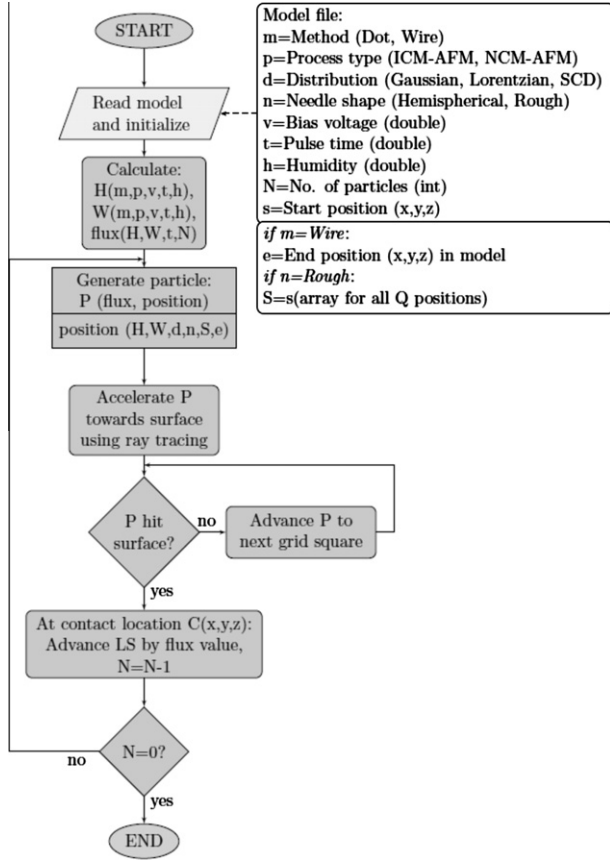


Fig. 8. Flow chart of the simulation process implementing the Monte Carlo method with ray tracing in a LS environment.

Eq. (29) is used in order to generate a one-dimensional probability density function (PDF)

$$f_{mc}(r_n) = -C \frac{DQ}{2\pi(r_n^2 + D^2)^{3/2}}, \quad (30)$$

where C is the normalization constant. C is found by integrating $f_{mc}(r_n)$ over the entire simulation domain and equating it to unity:

$$\int_{-\infty}^{\infty} f_{mc}(r_n) dr_n = -C \int_{-\infty}^{\infty} \frac{DQ}{2\pi(r_n^2 + D^2)^{3/2}} dr_n = 1. \quad (31)$$

Solving (31), we find that $C = -\pi D/Q$, which is then substituted into (30) to form the normalized PDF for a one-dimensional SCD distribution

$$f_{mc}(r_n) = \frac{D^2}{2(r_n^2 + D^2)^{3/2}}. \quad (32)$$

From (32) it can be seen that the normalized radial distribution is independent of the applied charge Q . The effect of the applied voltage is included in the nanodot growth through (21) and (23).

The next step is finding the cumulative probability distribution (CPD) function, derived by integrating the normalized PDF, $\Phi(r) = \int_{-\infty}^r f_{mc}(r_n) dr_n$, where r is the SCD distributed radius. Because of the symmetry of the SCD distribution on either side of the charged particle Q , generating a CPD distributed radius becomes easier, when $-0.5 \leq \Phi \leq 0.5$. Therefore, we set $\Phi(r) = \int_0^r f_{mc}(r_n) dr_n$, leading to

$$\Phi(r) = \xi_{mc} = \frac{r}{2\sqrt{r^2 + D^2}}. \quad (33)$$

Setting $\Phi(r)$ equal to an evenly distributed random number $\xi_{mc} \in (-0.5, 0.5)$ and inverting (33) allows to obtain the SCD quantile function required for particle generation:

$$r = 2D \frac{\xi_{mc}}{\sqrt{1 - 4\xi_{mc}^2}}. \quad (34)$$

Therefore, in order to generate particles obeying the SCD distribution along the silicon wafer surface, each particle must be generated using (34), where ξ_{mc} is an evenly distributed random number, $\xi_{mc} \in (-0.5, 0.5)$.

6.1.2. Two-dimensional surface charge density distribution

When working with a three-dimensional model for AFM nanodots, a two-dimensional particle distribution is required. The analysis is similar to the one-dimensional model presented in the previous section. The derivation of the quantile function is performed using polar coordinates for simplicity and for easier generation of a final radial distribution of particles. For polar coordinates (r_n, θ) it is important to note that the integration is performed through thin slices of the surface area, given by $r_n dr_n d\theta$. The normalization constant C is found by the same procedure used for the one-dimensional model, to be $C = -1/Q$ and the normalized two-dimensional PDF becomes

$$f_{mc}(r_n, \theta) = \frac{D}{2\pi(r_n^2 + D^2)^{3/2}}. \quad (35)$$

Once again, we note that the normalized radial distribution is independent of the applied charge Q .

The CPD is found by integrating the normalized PDF over the simulation area. The angular component results in a value of 2π , while the radial component is obtained by first finding the radial-dependent CPD

$$\Phi(r) = \int_0^{2\pi} \int_0^r f_{mc}(r_n, \theta) r_n dr_n d\theta, \quad (36)$$

which equates to

$$\Phi(r) = \xi_{mc} = 1 - \frac{D}{\sqrt{D^2 + r^2}}. \quad (37)$$

The quantile function for the two-dimensional SCD distribution is found by inverting the CPD function to obtain

$$r = D \sqrt{\frac{1}{(1 - \xi_{mc})^2} - 1}, \quad (38)$$

where ξ_{mc} is an evenly distributed random number, $\xi_{mc} \in (0, 1)$.

6.2. Rough and blunt needle tips

As mentioned in [12], in order to simulate the nanodot growth, initiated using a rough AFM tip, the needle can be modeled as a ring of charges at a given height above the silicon surface, as shown in Fig. 9.

The ring of charges is modeled by a desired number of dot charges surrounding the AFM tip circumference. When multiple dot charges are used to represent the AFM needle, the equation for the surface charge density becomes

$$\sigma(x, y, 0) = -\frac{D}{2\pi} \sum_{i=1}^N \frac{Q_i}{[(x - x_i)^2 + (y - y_i)^2 + D^2]^{3/2}}, \quad (39)$$

where N is the total number of charged dots, Q_i and (x_i, y_i, D) are the effective charge and the location of the i th dot, respectively, and $Q_i = Q/N$. The maximum possible SCD distribution occurs, when

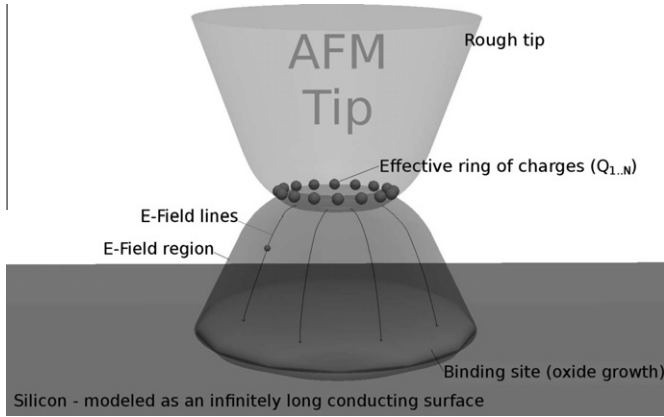


Fig. 9. Modeling approach for a rough AFM needle tip using a ring of charges to model the AFM needle.

all the charges are concentrated at a single point, making the charged circle's radius zero:

$$\sigma_{\max} = N \frac{Q}{2\pi D^2}, \quad (40)$$

where Q is the sum of all charges Q_i . When the charges along the charged ring are distributed evenly, the maximum surface charge density will depend on the ring's radius r_m and will appear at a location on the surface which is below one of the charges. Therefore, assuming the application of a blunt AFM needle, centered at (x_c, y_c) , the maximum surface charge density, to be used as a test for the Monte Carlo acceptance–rejection technique is given by

$$\sigma_{\text{ring,max}} = \frac{Q_1}{2\pi D^2} + \frac{D}{2\pi} \sum_{i=2}^N \frac{Q_i}{[(x_c - x_i + r_m)^2 + (y_c - y_i)^2 + D^2]^{3/2}}. \quad (41)$$

Although (41) gives a significantly more complex estimate for σ_{\max} , when compared to (40), the value obtained is the exact maximum and more test values will be accepted when the acceptance–rejection technique is applied, as suggested in [22] resulting in an overall quicker simulation. Although (40) is applicable regardless of how the charged dots are distributed along the AFM needle tip, using (41) improves the efficiency of the selection algorithm by a factor

of $\sigma_{\max}/\sigma_{\text{ring,max}}$ when the charged dots all have equal charge and are evenly distributed along the needle radius.

6.2.1. Monte Carlo acceptance–rejection technique

The SCD in (39) does not allow for a straight-forward derivation of a random particle distribution, such as the one shown in (34) and (38). Therefore, the Monte Carlo acceptance–rejection technique is applied [22], whereby a test point is generated on the entire simulation domain using an even distribution for x_t and y_t , $\xi(x_t, y_t)$. The surface charge density $\sigma(x_t, y_t, 0)$ is then calculated from (39). The idea behind the acceptance–rejection technique is to generate random variables, or particles, whose location follows (39) without having to derive an explicit equation for the quantile function. An evenly distributed random number ξ_σ is then generated in the range $(0, \sigma_{\max})$ or $(0, \sigma_{\text{ring,max}})$. This ensures that the maximum possible value of ξ_σ is larger than $\sigma(x_t, y_t, 0)$ for all test points (x_t, y_t) in the simulation domain. The generated test particle is accepted or rejected, depending on the relationship between ξ_σ and $\sigma(x_t, y_t, 0)$:

$$\begin{cases} \xi_\sigma \leq \sigma(x_t, y_t, 0), & \text{Accept } \tilde{\xi}(x_t, y_t), \\ \xi_\sigma > \sigma(x_t, y_t, 0), & \text{Reject } \tilde{\xi}(x_t, y_t). \end{cases} \quad (42)$$

When a particle location is rejected, a new particle is simulated and the procedure continues until a desired number of particles have been accepted to take part in the topography simulation. A comparison between nanodots generated using a hemispherical and rough needle tip with a radius of 1.5 nm, 3 nm, 5 nm, and 10 nm is shown in Fig. 10. The simulations were carried out for 0.125 ms with the bias voltage $V_b = 20$ V and humidity $h_r = 55\%$. It is evident that a blunt needle tip will result in a blunt nanodot formation with a slight increase in lateral spreading. As the radius of the charged ring is increased, a volcano-shaped nanodot begins to take shape, as noted in [12].

7. Sample simulations

The nanodots, created using an AFM in NCM and shown in Figs. 11–13 are generated using the presented technique. The height and FWHM of the nanodots are obtained using the empirical Eqs. (21) and (23), while the radial nanodot heights are a result of the implemented SCD particle distribution. In the figures, the top topography represents the surface between the silicon dioxide

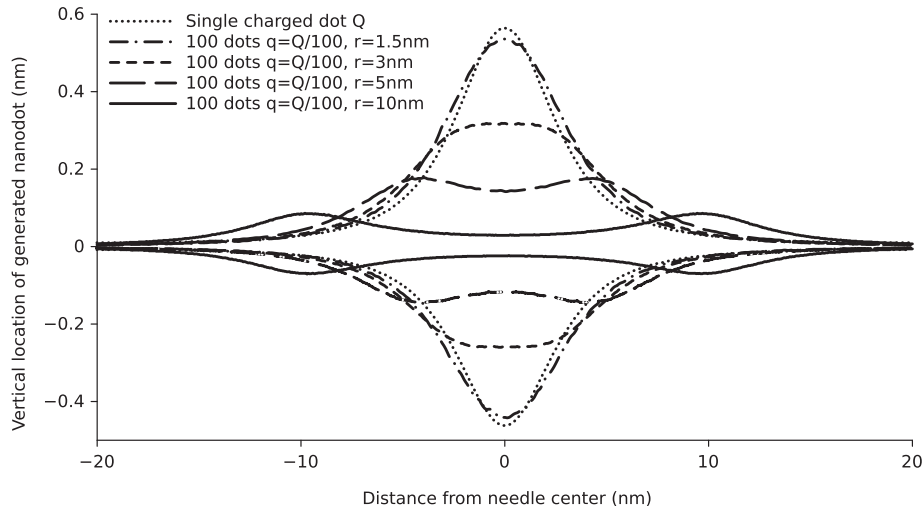


Fig. 10. Nanodot cross-sections generated using a hemispherical and a blunt AFM needle tip model. The hemispherical needle tip is modeled with a charge Q while the rough needle is modeled with a ring of 100 charges, each having a charge $0.01Q$. Several rough needle radii are shown – 1.5 nm, 3 nm, 5 nm, and 10 nm.

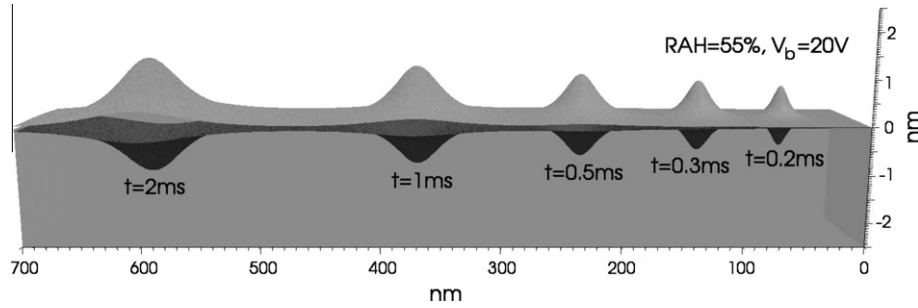


Fig. 11. Effects of pulse time on the nanodot height and width.

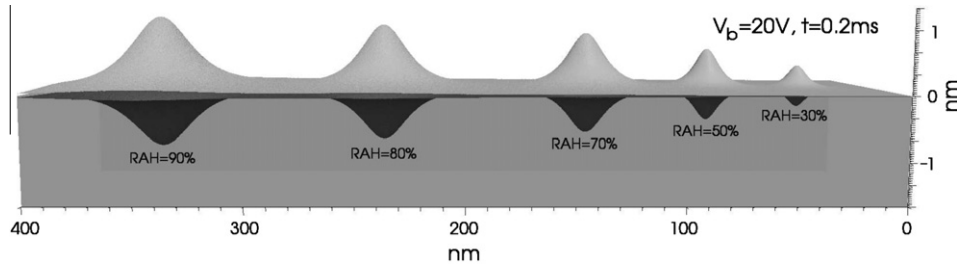


Fig. 12. Effects of ambient humidity on the nanodot height and width.

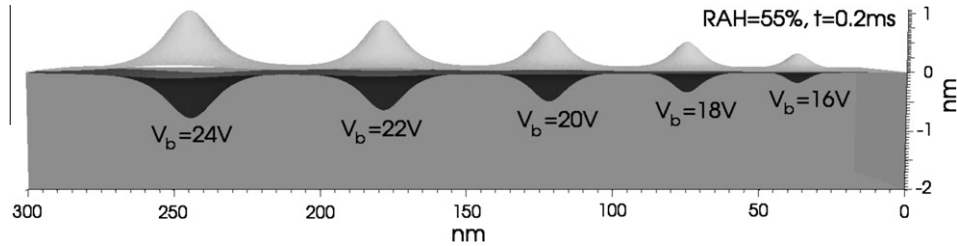


Fig. 13. Effects of bias voltage on the nanodot height and width.

and the air/water ambient, while the bottom topography represents the interface between silicon dioxide and silicon. The results confirm the experimental results gathered from [23,24], on which the empirical models are based.

The models reflect the experimentally observed logarithmic dependence of pulse time on the nanodot height and width, while the voltage dependence is relatively linear. The minimum humidity required in order to generate nanodots is 30%, while a minimum bias voltage of 4 V is required to generate a noticeable nanodot height. However, in order to use low voltages (<10 V) a longer pulse time (>0.2 s) must be applied, while for higher voltages (>20 V), a minimal pulse time (~ 0.1 ms) is sufficient.

The implemented model can be used to predict the nanodot topography within a wide range of ambient conditions including humidity from 30% to 100%, bias voltages larger than 4 V, and pulse times longer than 0 s. A 1 nm nanodot height can be achieved by applying a bias voltage of 20 V for 0.125 ms in a 55% humidity environment.

Fig. 11 shows the distribution of nanodot sizes caused by a variation of pulse times. The voltage and humidity were kept constant at 20 V and 55%, respectively, while the time was set to 0.2 ms, 0.3 ms, 0.5 ms, 1 ms, and 2 ms. With increasing pulse times, the nanodot height and width also increase, as expected. The height varies from 1.24 nm to 2.39 nm, while the FWHM varies from 15 nm to approximately 63 nm with pulse times set to 0.2 ms and 1 ms, respectively.

Fig. 12 shows the distribution of nanodot sizes caused by a variation of the ambient humidity. The pulse time and applied voltage

were kept constant at 0.2 ms and 20 V respectively, while the humidity was set to 30%, 50%, 70%, 80%, and 90%. With an increasing ambient humidity, the nanodot height and width also increase, as expected. The height varies from 0.65 nm to 2.07 nm, while FWHM varies from 10.6 nm to approximately 34 nm with the ambient humidity set to 30% and 90%, respectively.

Fig. 13 shows the distribution of nanodot sizes caused by a variation of the applied voltage. The pulse time and humidity were kept constant at 0.2 ms and 55%, respectively, while the voltage was varied at 16 V, 18 V, 20 V, 22 V, and 24 V. With an increasing applied voltage, the nanodot height and width also increase, as expected. The height varies from 0.51 nm to 1.91 nm, while FWHM varies from 10 nm to approximately 20.63 nm with the applied voltage set to 16 V and 24 V, respectively.

8. Summary

A simulation technique for local oxidation nanolithography of silicon with an Atomic Force Microscope in non-contact mode has been presented. The simulator is based on observing the electric field and ion concentrations at the oxide/silicon interface and generating oxide growth which is based on the distribution of charges at the surface.

For thick oxides, larger than several nanometers, three surfaces have been taken into consideration: ambient/oxide, oxide/trap site, and oxide trap site/silicon. The potential, electric field, and ion concentrations are solved for each surface boundary in order to

determine the final ion concentration at the oxide trap site/silicon interface, which is the main factor in deciding the oxide growth rate. An empirical model for the oxide thickness as a function of process time is presented, which is used in the simulator in order to estimate the locations of all surface boundaries during the surface rate calculation.

For very thin oxides which grow to a total height of up to several nanometers, the bias voltage is applied for only short bursts (<10 ms). If the native oxide is removed prior to the application of the charged AFM needle, only a single interface exists between the ambient and the silicon surface. Due to the short time scale and the small oxide heights produced, the simulation is carried out using a particle distribution assuming the influence of only the electric field in the liquid ambient. The surface charge density at the silicon surface is deduced from the electric field and the nanodot is grown according to this distribution.

A Monte Carlo technique for particle distribution according to the surface charge density is also presented for two-dimensional and three-dimensional simulations. When a rough or blunt AFM needle tip is used for surface patterning, a ring of charges around the needle's circumference is used instead of a dot charge to simulate the generated electric field. Using this method, a variety of needle shapes can be simulated within this environment, dependent only on the location of the dot charges.

References

- [1] R. García, R.V. Martínez, J. Martínez, *Chemical Society Review* 35 (1) (2006) 29–38.
- [2] D. Stiévenard, B. Legrand, *Progress in Surface Science* 81 (2–3) (2006) 112–140.
- [3] G. Binnig, H. Rohrer, EU patent number 0027517: Scanning apparatus for surface analysis using vacuum-tunnel effect at cryogenic temperatures (issued 29 April 1981).
- [4] G. Binnig, C.F. Quate, C. Gerber, *Physical Review Letters* 56 (9) (1986) 930–933.
- [5] J. Dagata, J. Schneir, H. Harary, C. Evans, M. Postek, J. Bennett, *Applied Physics Letters* 56 (20) (1990) 2001–2003.
- [6] H.C. Day, D.R. Allee, *Applied Physics Letters* 62 (21) (1993) 2691–2693.
- [7] R. García, M. Calleja, F. Perez-Murano, *Applied Physics Letters* 72 (18) (1998) 2295–2297.
- [8] R.V. Martínez, J. Martínez, R. García, *Nanotechnology* 21 (24) (2010) 245301. 5.
- [9] J.H. Lee, J.J. Ahn, A. Hallén, C.-M. Zetterling, S.M. Koo, *Materials Science Forum* 717–720 (2012) 905–908.
- [10] M. Nakamura, *Japanese Journal of Applied Physics* 50 (3) (2011) 5202.
- [11] A. Oriens, C. Clemons, D. Golovaty, G. Young, *Surface Science* 600 (16) (2006) 3297–3312.
- [12] S. Djurkovic, C. Clemons, D. Golovaty, G. Young, *Surface Science* 601 (23) (2007) 5340–5358.
- [13] J.A. Sethian, *Level Set Methods and Fast Marching Methods*, 2nd ed., Cambridge University Press, 1999.
- [14] O. Ertl, S. Selberherr, *Computer Physics Communications* 180 (8) (2009) 1242–1250.
- [15] Sentaurus Topography: Advanced Topography Simulator, Available from: <<http://www.synopsys.com/Tools/TCAD/CapsuleModule/sentaurustopods.pdf>>.
- [16] Synopsys, Inc.: Sentaurus Process, TSUPREM-IV, available from: <<http://www.synopsys.com/Tools/TCAD/ProcessSimulation/Pages/default.aspx>>.
- [17] L. Filipovic, S. Selberherr, in: K.K. Sabelfeld, I. Dimov (Eds.), *Monte Carlo Methods and Applications*, DeGruyter Proceedings in Mathematics, Walter de Gruyter, 2012, pp. 97–104.
- [18] A. Notargiacomo, A. Tseng, in: *IEEE Conference on, Nanotechnology*, 2009, pp. 907–910.
- [19] J. Huang, C.-L. Tsai, A.A. Tseng, *Journal of the Chinese Institute of Engineers* 33 (1) (2010) 55–61.
- [20] L. Filipovic, S. Selberherr, in: *Proceedings of the International Symposium on Microelectronics Technology and Devices (SBMicro)*, Brasilia, Brazil, 2012, pp. 265–272.
- [21] G. Mesa, E. Dobado-Fuentes, J.J. Saenz, *Journal of Applied Physics* 79 (1) (1996) 39–44.
- [22] I.T. Dimov, *Monte Carlo Methods for Applied Scientists*, World Scientific Publishing Co. Pte. Ltd., 2008.
- [23] M. Calleja, R. García, *Applied Physics Letters* 76 (23) (2000) 3427–3429.
- [24] T.-H. Fang, *Microelectronics Journal* 35 (9) (2004) 701–707.